University of Huddersfield Repository

Chen, Xiaomei, Longstaff, Andrew P., Fletcher, Simon and Myers, Alan

Deployment and evaluation of a dual-sensor autofocusing method for on-machine measurement of patterns of small holes on freeform surfaces

Original Citation

Chen, Xiaomei, Longstaff, Andrew P., Fletcher, Simon and Myers, Alan (2014) Deployment and evaluation of a dual-sensor autofocusing method for on-machine measurement of patterns of small holes on freeform surfaces. Applied Optics, 53 (10). pp. 2246-2255. ISSN 1559-128X

This version is available at http://eprints.hud.ac.uk/id/eprint/19917/

The University Repository is a digital collection of the research output of the University, available on Open Access. Copyright and Moral Rights for the items on this site are retained by the individual author and/or other copyright owners. Users may access full items free of charge; copies of full text items generally can be reproduced, displayed or performed and given to third parties in any format or medium for personal research or study, educational or not-for-profit purposes without prior permission or charge, provided:

- The authors, title and full bibliographic details is credited in any copy;
- A hyperlink and/or URL is included for the original metadata page; and
- The content is not changed in any way.

For more information, including our policy and submission procedure, please contact the Repository Team at: E.mailbox@hud.ac.uk.

http://eprints.hud.ac.uk/

Deployment and evaluation of a dual-sensor autofocusing method for on-machine measurement of patterns of small holes on freeform surfaces

Xiaomei Chen[1*], Andrew Longstaff[1], Simon Fletcher[1], and Alan Myers[1]

[1]*Centre for Precision Technologies, University of Huddersfield, Queensgate, Huddersfield HD1 3DH United Kingdom*
**Corresponding author: x.chen2@hud.ac.uk*

Received Month X, XXXX; revised Month X, XXXX; accepted Month X, XXXX;
posted Month X, XXXX (Doc. ID XXXXX); published Month X, XXXX

This paper presents and evaluates an active dual-sensor autofocusing system that combines an optical vision sensor and a tactile probe for autofocusing on arrays of small holes on freeform surfaces. The system has been tested on a two-axis test rig and then integrated onto a three-axis CNC milling machine, where the aim is to rapidly and controllably measure the hole position errors while the part is still on the machine. The principle of operation is for the tactile probe to locate the nominal positions of holes and the optical vision sensor follows to focus and capture the images of the holes. The images are then processed to provide hole position measurement. In this paper, the autofocusing deviations are analyzed. First, the deviations caused by the geometric errors of the axes on which the dual-sensor unit is deployed. are estimated to be 11 μm when deployed on test rig and 7 μm on the CNC machine tool. Subsequently, the autofocusing deviations caused by the interaction of the tactile probe, surface and small hole are mathematically analyzed and evaluated. The deviations are a result of the tactile probe radius, the curvatures at the positions where small holes are drilled on the freeform surface and the effect of the position error of the hole on focusing. An example case study is provided for the measurement of a pattern of small holes on an elliptical cylinder on the two machines. The absolute sum of the autofocusing deviations is 118 μm on the test rig and 144 μm on the machine tool. This is much less than the 500 μm depth of field (DOF) of the optical microscope. Therefore, the method is capable of capturing a group of clear images of the mall holes on this workpiece for either implementation.
© 2012 Optical Society of America
OCIS codes: (120.0120) Instrumentation, measurement, and metrology; (110.0110) Imaging systems; (150.0150) Machine vision.
http://dx.doi/org/10.1364/AO.99.099999

1. Introduction

In the automotive, aviation and space industries, there are increasing demands for the inspection and measurement of small through-holes, blind-holes and taper-holes etc. within Ø 1 mm on freeform surfaces. For example, arrays of 79 air-cooling holes on a freeform aero-engine blade have diameters between 0.3 mm and 0.5 mm. Their positional tolerance is ±11 arcmin to ensure uniform distribution of cooling airflow. Measurement of so many small features is simply too difficult to be accessed with a tactile probe of a coordinate measuring machine (CMM) or computer numerical control (CNC) machine tool. Other probes for nano- and micro-metrology [1], especially the tactile optical-fibre probe [2] for the measurement of small holes, are too fragile and costly to measure such a large number of small holes in a production environment. An optical vision sensor that consists of a high-resolution digital camera and an optical microscope (a set of objective lens) allows performing such measurements by means of image processing and vision inspection technology. This technology has been broadly applied in various measurement fields, such as the inspection and measurement of hole position and orientation on a flat surface, a circular cylinder and a sphere which all have regular shape and equal curvature [3,4]; the inspection of the form and profile of a workpiece [5,6]; the discovery and measurement of surface defects [7]; the isolation and measurement of the features that arrays of cell aggregate [8]; and wheel steer angle detection [9].

A clear image is necessary when using an optical vision sensor for measurement and inspection. Autofocussing is essential for efficient measurement and good repeatability. The autofocusing techniques currently used mainly rely on the various optical evaluation functions (OEF) [10-12]. In practice, the optical microscope is driven to move in increments from a short distance below the focal plane to a short distance above the focal plane while a series of images are captured at different heights. The corresponding series of OEF values are calculated and the plane whose image corresponds to the maximum of the OEF is approximately the focal plane. The procedure uses a hill-climbing search algorithm [13], which is ultimately limited by the resolution of the separation of the planes. CMMs equipped with an optical vision sensor usually employ such autofocusing methods.

2. Limitations of Single Optical Vision Sensor Autofocusing

OEF-based methods can be successfully applied when autofocussing on features on a flat surface. However, the method is less successful when focusing on features such as small holes drilled on the steep slope of a freeform surface. The method is highly sensitive to the illuminating light intensity, the reflectivity of the

illuminated workpiece surface and the depth of field (DOF) of the optical microscope. Thus, the focus positions have to be manually selected, which is time-consuming and less repeatable since it is subject to the skill-level of the operator.

An example of the limitations of OEF-based autofocussing is the inspection of a small hole on a turbine blade. The light-reflecting condition on the surface of the turbine blade introduces a significant level of noise, while the illuminating light reflects at different angles along the surface depending upon the curvature at each point. The OEF-based autofocusing method can find false solutions, as shown in Fig.1, where ambiguity exists while autofocussing on the outer border of a small hole drilled on the more skewed slope of the blade. If the optical microscope lens moves vertically to position C_1, the lower half of the ellipse image is clear and upper half of it blurs; if the optical microscope lens moves vertically to position C_2, the upper half of the ellipse image is clear while the lower half of it blurs. Between positions C_1 and C_2, the location of the focal plane is ambiguous, with the uncertainty increasing as the steepness of the slope increases.

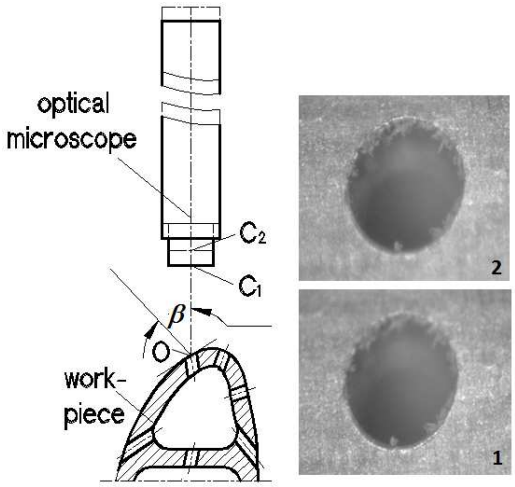

Fig. 1. Ambiguity by only optically focusing the small hole on a turbine blade surface at lens position C_1 and C_2: corresponding image 1 and 2 are blurred in upper/lower semicircle and clear in opposite semicircle.

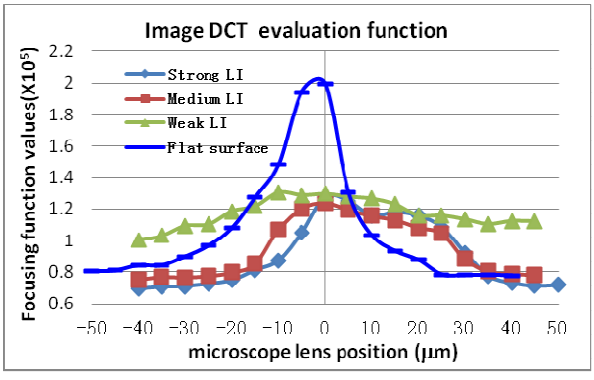

Fig. 2. Focusing curves based on image DCT evaluation function for a hole on an elliptic cylinder shell under different illuminating light intensity (LI) and a hardness indentation on a flat workpiece.

During this work, several typical OEF methods were tested by focusing on a small hole on an elliptic cylinder and a Brinel hardness indentation on a flat workpiece using the hill-climbing search procedure. The tested methods include the image entropy function [14], image gradient variance evaluation function [15] and image discrete cosine transformation (DCT) evaluation function [16]. A series of images were captured with varying illuminating light intensity (LI), which was tuned to be strong, medium and weak for the elliptic cylinder and medium for the flat workpiece. The values of the OEF were calculated from the corresponding images that were taken when the optical microscope lens was moved at equal step length starting from beneath the focal plane and finishing above the focal plane. The ideal "focusing curve" versus "lens position" should have a single peak with two mathematically monotonic sides; the steeper the side is, the higher the focusing resolution is and so the sharper the image contrast [16].

The DCT evaluation was found to be the most capable focusing evaluation function tested, so itis taken as the example to explain the problem of autofocusing using a single optical vision sensor based on the OEF. A series of images at 5 μm intervals were taken by a microscope with approximately 100 μm DOF. The focusing values of the DCT evaluation function were calculated from the different images corresponding to different positions. The values are plotted in Fig. 2. Since the two workpieces are not at the same height, the starting vertical positions are different for the two samples. The vertical position of an image with the maximum DCT value is approximately the true focal plane, so Fig. 2 has this position as the zero microscope lens position. Consequently, the other vertical positions of the images that are either higher or lower than this zero are presented as negative or positive positions respectively. The DCT curve for the hardness indentation on the flat workpiece appears much sharper than a hole on the elliptical cylinder, emphasising the limitations in transferring this method to the more complex surface. Similarly, the effect of LI on the focussing of the elliptical cylinder is significant, clearly showing the problem of non-repeatability of this method on this type of parts under varying conditions.

3. Dual-sensor autofocusing

To overcome the limitations associated with OEF-based focusing, this paper proposes an active, fixed-focusing method for the automatic measurement of the positions or orientations of arrays of small holes on freeform surfaces. The system works by combining an optical vision sensor and a tactile probe. The tactile probe locates the surface height at the position of each of the holes in its sensing direction and feeds back the required offset to the control unit for the optical vision sensor, which can then be driven to the required focusing position. A prerequisite for the dual-sensor autofocusing method is prior knowledge of the focal plane of the optical microscope, which can be found from its technical specifications or, more accurately, by practical calibration. The principle is that the distance, $\boldsymbol{L}$, between the point of measurement of the tactile probe and the lens of optical microscope must be a known amount from the object distance, $\boldsymbol{L_O}$, of the optical microscope. In practice, it is most efficient to set $\boldsymbol{L}$ equal to $\boldsymbol{L_O}$. The two sensors must be assembled into one holder either parallel to each other with a known distance, $\boldsymbol{d}$, as shown in Fig. 3 (a) or perpendicular to each other as shown in Fig. 3 (b). The perpendicular configuration requires a rotary axis to swap between the two sensors. The *XOZ* in Fig.3 is the measurement coordinate system in the plane of the displacement of the two sensors. In this

plane the sensors are either displaced (parallel configuration) or swapped (perpendicular configuration). The *XOZ* system takes the rotary stage center as the coordinate origin for that plane, which is coincident with that of the workpiece. The *Y*-axis is perpendicular to the other two axes to complete the Cartesian coordinate system. Taking the parallel configuration in Fig. 3(a) as an example, the autofocusing and measurement procedure is described below.

The first operation uses the tactile probe. Starting from the datum hole, which is usually defined on the design drawing, the tactile probe is used sequentially to probe the relative position (focal plane) of each hole in the direction parallel to the axis of the optical sensor. To achieve this, the rotary stage rotates the workpiece by the nominal angle of rotational separation, α, until each hole comes underneath the tactile probe in turn. In the second operation, the optical vision sensor is translated by $\boldsymbol{d}$ (parallel configuration) or introduced (perpendicular configuration). It is then controlled to track the relative vertical position of each small hole, as determined in the first operation, as the workpiece is rotated to the same rotationally sequential positions. This control method establishes the focussing of the optical vision sensor and so captures the image of each small hole, one by one.

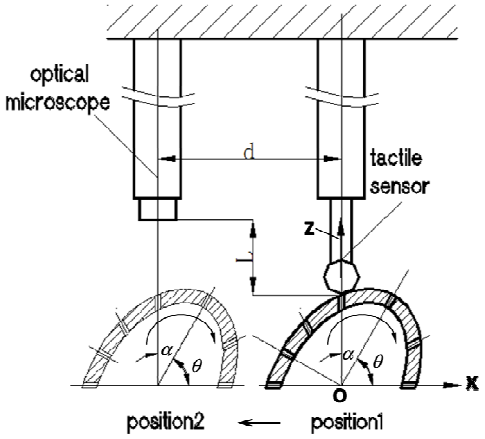

(a)

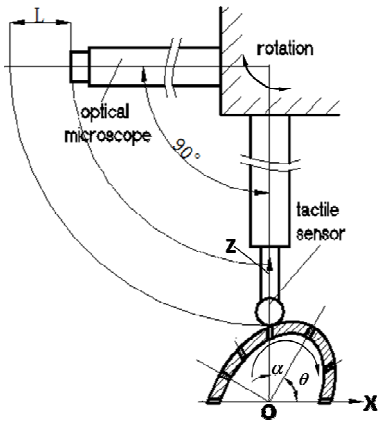

(b)

Fig. 3. Dual-sensor autofocusing configurations with (a) parallel and (b) perpendicular to each other.

Some multi-sensor CMMs that are equipped with two or more Z-axes that can load an optical sensor and a tactile probe concurrently [2, 17] could perform the dual-sensor autofocusing method, although it is unlikely that they could perform the automated method proposed without some hardware or software modification. Other commercially available multi-sensor CMMs have one z-axis and can load only one probe at a time. A single Z-axis is a disadvantage for performing the proposed method, unless the devices can be simultaneously mounted, since the act of changing the sensors increases measurement time and introduces additional measurement uncertainty.

4. Analysis of autofocussing deviation due to translation axes

A parallel dual-sensor-autofocusing configuration was produced to prove the concept of the system in a temperature controlled measurement laboratory before integration on a CNC milling machine in a standard workshop environment. The optical vision sensor is made up of an optical microscope with tuneable optical magnification and 500 µm depth of field (DOF), a coaxial LED ring-light mounted at its objective end and a CCD camera connected to it at its image end. The tactile probe could be a standard CMM or CNC machine tool probe or could be of bespoke design. The two applications are described in the following section 4A and 4B.

A. Dual-sensor autofocusing unit on a two-axis test rig

Previous work [18] introduced the combination of the optical vision sensor and a contact inductive sensor (CIS) with its own electronics box. The CIS has *R* 1.5 mm probe radius, 0.01 µm resolution and 3.2 µm maximum permissible error (E_{MPE}) in the ±0.5 mm measuring range. Two sensors, through specially designed mechanical parts, were mounted onto the *Z*-axis of a test rig shown in Fig. 4. The rig consists of a 2D motorized *X*-*Z* translation stage and a rotary table. Together with the dual-sensor autofocusing unit, the test rig is completely computer-controllable.

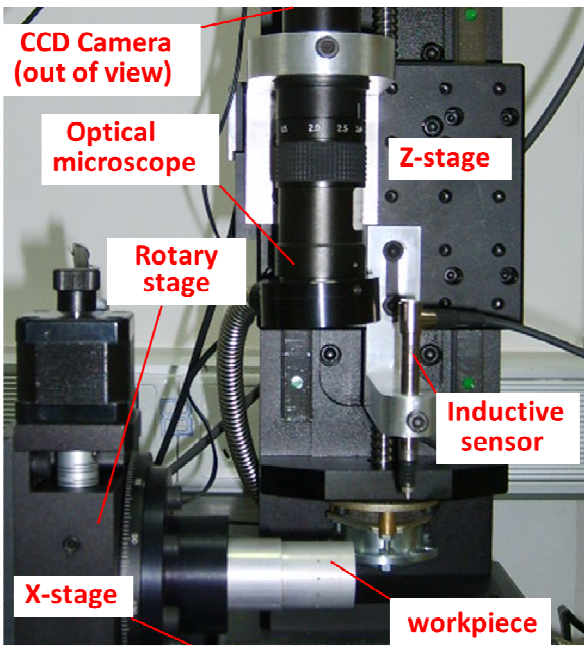

Fig. 4. Dual-sensor-autofocusing unit applied on the test rig.

The distance between two sensor axes d = 62.5 mm, working distance L = 95 mm. The positioning repeatability R_Z, positioning backlash B_Z, motion straightness errors (E_{XZ}, E_{YZ}, E_{ZX}, E_{YX}), parallelism (E_{PZ}, E_{PX}), yaw (E_{BZ}, E_{CX}) and pitch (E_{AZ}, E_{BX}) are ±3 µm, 5 µm, 10 µm/100 mm and 10 µm/100 mm, 15 arcsec and 15 arcsec respectively in 100 mm moving range for both the *X*-axis and *Z*-axis. Among the errors, E_r and E_B are the main errors that directly contribute to the autofocusing deviation, while E_{PX} and E_{BX} indirectly contribute to the focusing error. The remaining errors would influence the uncertainty of the position measurement of small holes. A rotary stage with 4.5 arcsec resolution and 18 arcsec positioning repeatability was mounted on the X-axis stage to rotate the workpiece. The autofocusing deviation contributed by *X*- and *Z*-stage and maximum permissible error of the CIS is 11.5 µm which is calculated by:

$$u_c(f) = [2R_Z^{\ 2} + 2B_Z^{\ 2} + E_{PX}^2(d) + E_{BX}^2(d) + E_{MPE}^2]^{1/2} \qquad (1)$$

where, $E_{PX}(d) = d \times E_{PX}$ =62.5 × 10/100=6.25 µm, $E_{BX}(d) = d \times E_{BX}$ × (1/3600) × (π/180) = 4 µm and digit '2' means that *Z*-stage travel forward one time and backward one time.

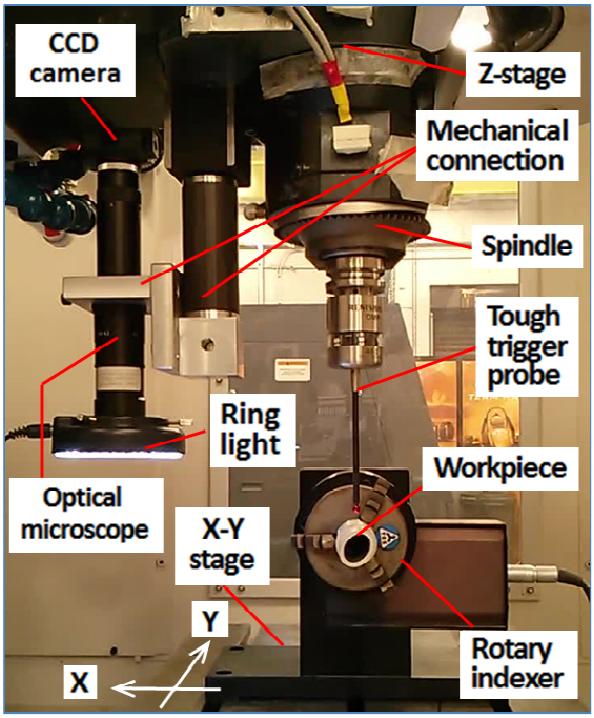

Fig. 5 Dual-sensor autofocusing unit applied on the machine tool,

B. Dual-sensor autofocusing unit on a CNC machine tool

In accordance with the schematic parallel configuration in Fig. 3(a), the optical vision sensor was mounted onto the Z-axis of a small 3-axis vertical machining center, as shown in Fig.5. The tough trigger probe is a Renishaw OMP 40-2 with stylus radius R 3 mm and 1 µm repeatability E_{RP}. Before installing the optical vision sensor, the accuracy and positioning repeatability of the axes of motion were calibrated using a multi-degree of freedom (MDF) laser interferometer according to ISO 230-2:2011 [19] and ISO 230-1:2012 [20]. The related errors were as follows:

- *Z*-axis and *X*-axis motion positioning errors E_{ZZ} and E_{XX} were 14.1µm in 300 mm range and 11.3µm in 400 mm range. *Z*-axis and *X*- axis positioning repeatability R_Z and R_X are ± 3.5 µm and ± 3.3 µm. *Z*-axis and *X*-axis reversal (backlash) B_Z and B_X are 1.2 µm and 2.3 µm.
- *Z*-axis motion straightness errors in the *X*- and *Y*-direction, E_{XZ} and E_{YZ}, are 3.3 µm/300 mm and 3.6 µm/400 mm. *X*-axis motion straightness errors in the Z- and Y-direction, E_{ZX} and E_{YX}, are 4.7 µm/400 mm and 4.4 µm/400 mm.
- *Z*-axis motion angular errors around *X*- and *Y*-direction, E_{BZ} and E_{AZ}, are 1.8 arcsec and 6.1 arcsec. *X*-axis motion angular errors around *Y*- and Z-direction, E_{BX} and E_{CX}, are 4.9 arcsec and 68.4 arcsec.

Among the errors, E_{ZZ}, R_Z and B_Z are the main errors that directly contribute to the autofocusing deviation, while E_{XX}, E_{ZX} and E_{BX} indirectly contribute to the focusing error. The remaining errors would influence the uncertainty of the position measurement of small holes. E_{ZZ} and E_{XX} can be compensated using standard CNC software features. A Renishaw RX10 rotary indexer was installed on the *X*-*Y* stage to rotate the workpiece. It had a maximum position error of ±1 arc second for each 5° step rotary according to the calibration certificate. The 6.8 µm autofocusing deviation contributed by the *X*- and *Z*-stage and the repeatability of the probe is calculated by:

$$u_c(f) = [2R_Z^{\ 2} + 2B_Z^{\ 2} + E_{ZX}^2(d) + E_{BX}^2(d) + E_{RP}^2]^{1/2} \qquad \mathbf{(2)}$$

where, d is the distance between two sensor axes, and small d means that the related errors can decrease. Due to the robust and large calibre of spindle, d =150 mm; $E_{ZX}(d) = d \times E_{ZX}$ =150 × 4.7/400=1.8 µm, $E_{BX}(d) = d \times E_{BX} \times (1/3600) \times (\pi/180)$ = 3.6 µm.

5. Autofocusing deviations caused by the interaction of the tactile probe, surface and small hole

In addition to the geometric errors of the axes, the interaction between the probe radius, the radius of the measured hole and the curvature of the workpiece around the hole location are the main contributors to the autofocusing error. These errors are mathematically analysed in section 5A and5 B.

A. Small hole on protruding part of a freeform surface

When the tactile probe is used to locate the surface height near a small hole, the spherical stylus will tend to sink into the hole for a short distance, ***s***. This value varies in depth, depending on: the diameter of the tactile probe; the diameter of the hole; the curvature of the freeform surface at the outer edge of the small hole; and the offset of the probe from the center of the hole. Here we only consider the cases where the hole is drilled around the top of a convex area or at the bottom of the concave area. The influence of the radius of the tactile probe and the curvature of the freeform surface on autofocusing accuracy is shown in Fig. 6.

If the sphere radius of the tactile probe and small hole are R and r respectively, the stylus of the tactile probe is lower than the outline of the small hole by a distance of ***s***, therefore:

$$s = R - \sqrt{R^2 - r^2} \qquad (R > r) \qquad (3)$$

If the outline of a small hole on the freeform surface is not within one horizontal circle, but in a saddle or other loop, and if the height

between the top point and bottom point is ***t***, and the curvature radius of the freeform surface is ρ, then

$$t = \rho - \sqrt{\rho^2 - r^2} \qquad (\rho > r) \tag{4}$$

where, ρ is the absolute reciprocal of the curvature K: $\rho = |K^{-1}|$.

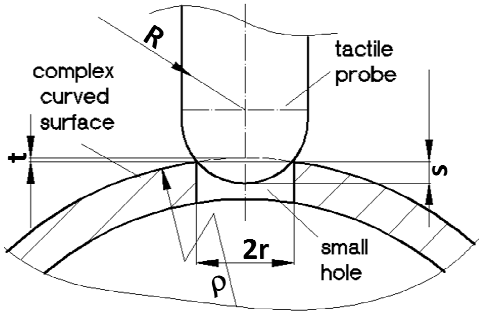

Fig. 6. Schematic of a tactile probe contacting a small hole on the protruding part of a freeform surface.

B. Hole on skewed and sloped part of a freeform surface

The geometrical interaction between the stylus of the tactile probe and the skewed and sloped part of a convex or concave freeform surface will result in a probing deviation which varies according to the skewedness and curvature at the contacted point on the freeform surface.

Following a detailed schematic of the geometrical relationship between the stylus radius R of the tactile probe and a 3D concave freeform surface with a small hole shown in Fig. 7(a), the focusing deviation can be derived.

If a freeform surface implicitly expressed by $F(X, Y, Z) = 0$ has continuous partial differentiations $F_X(X, Y, Z)$, $F_Y(X, Y, Z)$ and $F_Z(X, Y, Z)$ [21] at a point $p(X, Y, Z)$, the normal vector $\vec{n}$ at this point is

$$n = (F_x(X, Y, Z), F_y(X, Y, Z), F_z(X, Y, Z)) \tag{5}$$

For freeform surface explicitly expressed by $Z = f(X, Y)$, if setting $F(X, Y, Z) = f(X, Y) - Z$, then $F_X(X, Y, Z) = f_X(X, Y)$, $F_Y(X, Y, Z) = f_Y(X, Y)$ and $F_Z(X, Y, Z) = -1$. Thus, if the partial differentiations $f_X(X, Y)$ and $f_Y(X, Y)$ of function $f(X, Y)$ is continuous at a point $\boldsymbol{p}(X, Y, Z)$, the normal vector at this point expressed in equation (5 is modified to

$$n = (f_X(X, Y), f_Y(X, Y), -1) \tag{6}$$

In Fig. 7 (a), ***p*** is the actual contact point between the probe and the freeform surface; ΔZ is the deviation introduced by the probe radius R; p_E is the center of the probe stylus. The trace of the stylus center p_E with equal distance R from $Z = f(X, Y)$, can be express as

$$f_E(X, Y) = f(X, Y) + R \cdot \vec{n} \tag{7}$$

The cosine of the angle γ between the normal vector and z-axis direction is

$$\cos\gamma = Z / |\vec{n}| = 1 / \sqrt{f_X^2(X, Y) + f_Y^2(X, Y) + 1} \tag{8}$$

Therefore, the equation (7) can be rewritten as

$$f_E(X, Y) \approx f(X, Y) + R / \cos\gamma \tag{9}$$

The autofocusing deviation caused by the spherical probe radius is

$$\Delta Z = f_E(X, Y) - f(X, Y) - R \approx R(1/\cos\gamma - 1) \tag{10}$$

where γ is indeed the slope of point ***p*** on the freeform surface, and

$$\tan\gamma = [f_X^2(X, Y) + f_Y^2(X, Y)]^{1/2} \tag{11}$$

After combining equation (8), (9) and (10), the finally autofocusing deviation is

$$\Delta Z \approx R \cdot [(\tan^2\gamma + 1)^{1/2} - 1] \tag{12}$$

Ideally, to minimize the probing deviation ΔZ, R should be as small as possible in equation (13), as long as $R > r$.

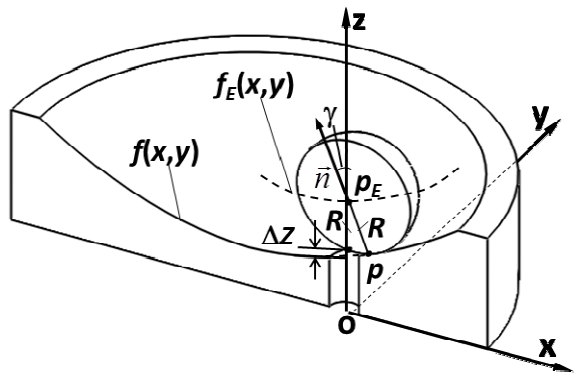

(a)

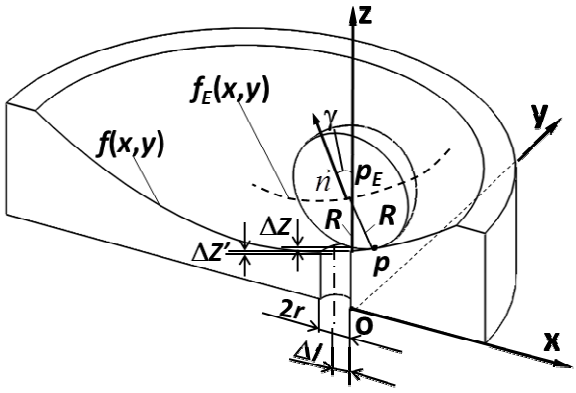

(b)

Fig.7. Schematic of autofocusing deviation caused by a tactile probe if it aligns on the freeform surface at (a) the centerline of the hole and (b) offset from the centerline.

If the actual position of the small hole deviates from the nominal as shown in Fig. 7 (b), the tactile probe will contact the surface either above or below the projected centerline of the hole. The diagram shows the case where the probe contacts the higher edge of the small hole. The linear position error of small hole, Δl, causes an additional autofocusing error $\Delta Z'$. $\gamma'$is the slope at the point where the surface intersects the Z-axis. Usually the probe radius R is much smaller than the curvature radius at the point p, $\gamma' \approx \gamma$. Therefore, the additional autofocusing error $\Delta Z'$ is expressed as

$$\Delta Z' = \Delta l \cdot \tan\gamma' \approx r \cdot \tan\gamma \tag{13}$$

Since the probing deviation will increase as Δl increases, we should consider additional compensation in the focusing algorithm on poorly manufactured parts.

The focusing deviations increase with the increases of both the tactile probe radius and the slopes around the locations of the small holes on the freeform surface. The focusing deviations ΔZ and $\Delta Z'$ need to be compensated if the radius is close to, or larger than, the DOF of optical microscope. This can be explained by considering

an example of an optical microscope measuring system with 500 μm DOF. For different tactile probe radii of 0.5 mm, 1.0 mm, 2.0 mm and 3.0 mm, the focusing deviations ΔZ and ΔZ′ will reach the DOF if the skewed angle at the higher edge of a small hole on the complex-curved surface has reached the thresholds listed in table 1.

Table 1 Thresholds of skewed angles at the higher edge of a small hole on a freeform surface.

R (mm) / Δl (mm)	0.5	1.0	2.0	3.0
0.25	45°	37.5°	30°	27.5°
0.5	35°	30°	25°	22.5°

For an array of small holes on a freeform surface whose design parameters are already known, the probe radius should be chosen based on the comprehensive consideration of focusing deviation ***s***, ***t*** and ΔZ and ΔZ′. Nevertheless, we can compensate those focusing deviations when making a measurement program, if the dual-sensor autofocusing unit is integrated into a machine tool or a controllable test rig. Compensation can be made by correcting the deviation ***s***, ***t*** and ΔZ and ΔZ′ from the height $|L\text{-}L_0|$. This means moving the optical microscope using the Z-axis stage by an extra displacement ($\Delta Z+\Delta Z' - s - t$), so that the related small hole can be clearly imaged by the optical microscope.

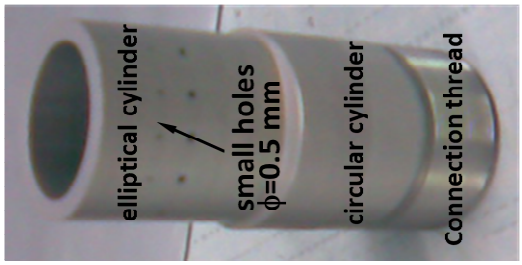

Fig 8 Elliptical cylinder shell

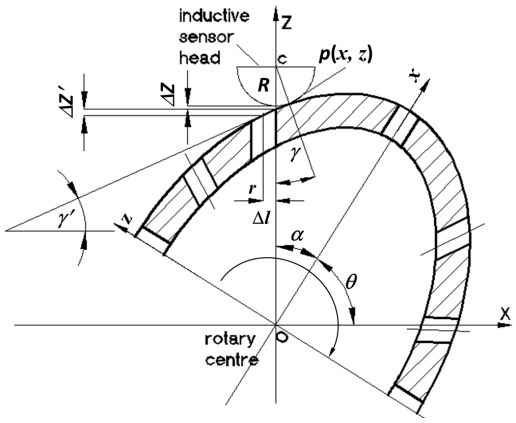

Fig. 9. Schematic of an inductive sensor head contacting a small hole on an elliptical cylinder

6. Autofocusing experiment

The autofocusing errors vary according to different freeform design. Therefore, an elliptical cylinder shell is used as an example to demonstrate how to analyse the autofocusing error. It has a 28 mm long axis ***a***, a 22.4 mm short axis ***b*** and 3 mm shell thickness. A pattern of Ø 0.5 mm small holes were centripetally drilled with regular angular distribution on its circumference shown in Fig. 8.

A. Focusing deviation evaluation

The schematic of a tactile probe contacting a small hole on the slope of elliptical cylinder shell is shown in Fig. 9. R and r represent the radius of the tactile probe and a small hole. The centreline of the tactile probe is in the Z-axis. The ellipse rotates an angle θ in the XOZ coordinate system. α is the nominal angle of any two adjacent small holes. If *xoz* represents the workpiece coordinate system, the coordinate of the contact point is (x, z). The ellipse formula is

$$\begin{cases} x = a \cdot \cos\alpha \\ z = b \cdot \sin\alpha \end{cases} \quad (0 \le \alpha < 2\pi) \tag{14}$$

The parametric function of the ellipse in *XOZ* coordinate system is expressed by

$$\begin{cases} X = x\cos\theta - z\sin\theta \\ Z = x\sin\theta + z\cos\theta \end{cases} \tag{15}$$

When the tactile probe contacts a hole, X=0 and $x\cos\theta = z\sin\theta$ in equation (15). Therefore,

$$\tan\theta = \frac{x}{z} = \frac{a}{b}\cdot\frac{\cos\alpha}{\sin\alpha} \tag{16}$$

The differentiation of Z with respect to X relates to γ:

$$\tan\gamma = \frac{dZ}{dX} = \frac{(dx/d\alpha)\cdot\sin\theta + (dz/d\alpha)\cdot\cos\theta}{(dx/d\alpha)\cdot\cos\theta - (dz/d\alpha)\cdot\sin\theta} \tag{17}$$

The combination equation (16) and equation (17) gives

$$\tan\gamma = \frac{a^2-b}{2ab}\sin(2\alpha) \quad (0 \le \alpha < \pi/2) \tag{18}$$

Focusing deviation ΔZ and ΔZ′ is respectively

$$\begin{aligned} \Delta Z &\approx R\cdot(\sqrt{1+\tan^2\gamma}-1) \\ &= R\cdot[(1+\frac{(a^2-b^2)^2}{4a^2b^2}\cdot\sin^2 2\alpha)^{\frac{1}{2}}-1] \end{aligned} \tag{19}$$

and

$$\Delta Z' \approx r\cdot\tan\gamma = r\cdot\frac{a^2-b^2}{2ab}\sin(2\alpha) \tag{20}$$

Since the first and second derivatives of the ellipse are

$$\begin{cases} \dfrac{dz}{dx} = -\dfrac{b}{a}\cot\alpha \\ \dfrac{d^2z}{dx^2} = \dfrac{b}{a^3\sin^3\alpha} \end{cases} \tag{21}$$

and the curvature of the ellipse is

$$\begin{aligned} K &= (\frac{d^2z}{dx^2})/(1+(\frac{dz}{dx})^2)^{3/2} \\ &= ab/(a^2\sin^2\alpha + b^2\cos^2\alpha)^{3/2} \end{aligned} \tag{22}$$

the curvature radius is

$$\rho = |K^{-1}| = \frac{1}{ab}\left|(a^2\sin^2\alpha + b^2\cos^2\alpha)^{3/2}\right| \tag{23}$$

If the small holes drilled at α= 45°, 135°, 225° and 315° are probed by the tactile probe, ΔZ and ΔZ′ reach their maximum. If the small

holes drilled at α = 0°, 90°, 180° and 270° are probed by the same tactile probe, ΔZ and $\Delta Z'$ diminish to their minimum.

r=0.25 mm, R=1.5 mm and 3 mm for contact inductive sensor and tough trigger probe. Therefore, the maximum focusing deviation ΔZ_{max}=38 µm for the contact inductive sensor whilst ΔZ_{max}=76 µm for the touch trigger probe; $\Delta Z'_{max}$=56 µm; the minimum focusing deviation $\Delta Z_{min}=\Delta Z'_{min}=0$.

If α = 45°, 135°, 225° and 315°, $t \approx 2$ µm; if α = 90° and 270°, $t \approx 1.8$ µm; if α = 0° and 180°, $t \approx 3$ µm.

$s \approx 21$ µm for the contact inductive sensor with R1.5 mm radius whilst $s \approx 10$ µm for the touch trigger probe with R 3 mm radius.

When also considering the autofocusing error $u_c(f)$ introduced by the machine, the total autofocusing deviation is calculated by

$$\begin{cases} \delta_{min} = -[s^2 + t^2 + u_c^2(f)]^{1/2} \\ \delta_{max} = [(\Delta Z + \Delta Z')^2 + u_c^2(f)]^{1/2} \end{cases} \quad (24)$$

A negative deviation means over-focusing and a positive deviation means under-focusing. It is between -23 µm and 95 µm for the configuration of dual-sensor autofocusing unit on the test rig; it is between -12 µm and 132 µm for the configuration of the dual-sensor autofocusing unit on the machine tool. The absolute sum of the autofocusing deviations is 118 µm on the test rig and 144 µm on the machine tool. Because the 500 µm depth of field (DOF) of the microscope is far beyond the focusing deviations, we can obtain a pattern of clear images of the small holes without compensating the autofocusing deviation.

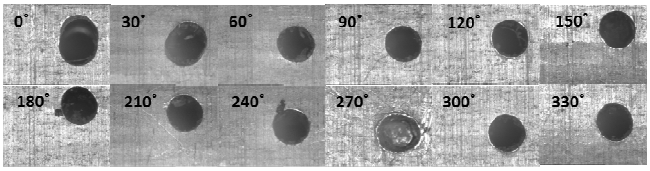

(a)

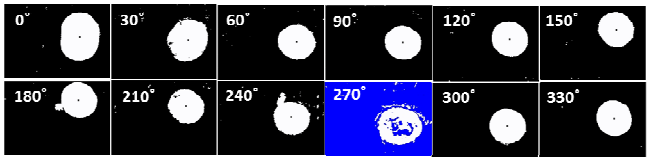

(b)

Fig. 10. (a) Images of a pattern of 12 small holes of Ø 0.5mm (3.5 times optical magnification) autofocused and captured on the test rig and (b) their binary images marked with the calculated centroids [18].

B. Autofocusing results

Fig.10 (a) and Fig. 11(a) show the captured images with 3.5 and 3.75 times magnification respectively. In each figure, the hole with legend 0° is one drilled on the long axis and is considered as the datum in the autofocusing procedure. The images are arranged so that they correspond from left to right with the axis (Y-axis) direction and from bottom to top with the circumferential (X-axis) direction of the elliptic cylinder shell. The cyclic trend in the locations of the imaged small holes is mainly due to the concentricity errors between the centerline of rotary stage and that of the workpiece. Furthermore, CMM measurement results indicate that the elliptic cylinder portion has concentricity errors of 30 µm in the long-axis and 10 µm in short-axis with reference to the circular cylinder portion. The centers of the small holes are found by segmenting the image into a binary image and then detecting the centroid of the small hole on the binary image [18]. This is achieved within a few milliseconds and the resultant measurements are shown in Fig. 10 (b) and Fig. 11(b).

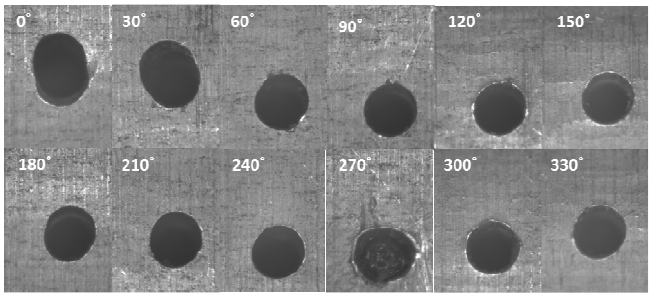

(a)

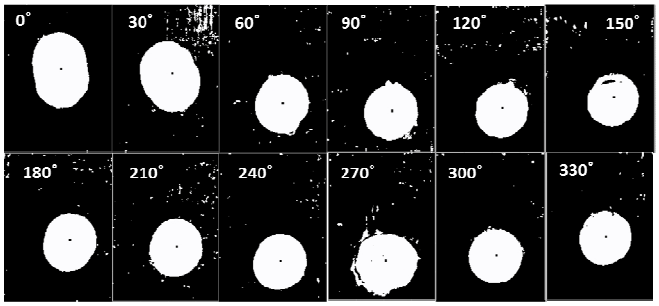

(b)

Fig.11. (a) Images of a pattern of 12 small holes of Ø 0.5 mm (3.75 times optical magnification) autofocused and captured on machine tool and (b) their binary images marked with the calculated centroids.

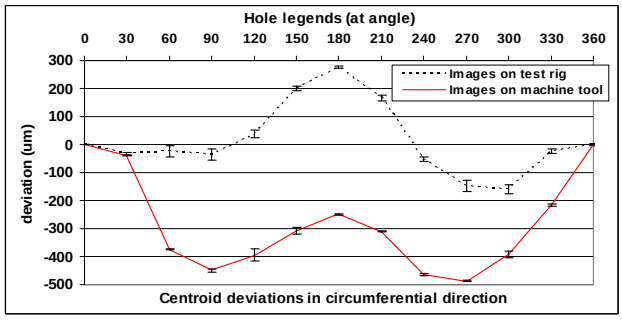

(a)

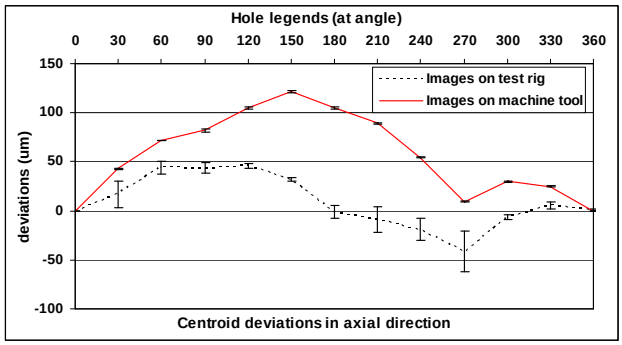

(b)

Fig. 12. Repeatability of detected deviations of hole centroid in directions of (a) circumference ($X_i - X_i'$) (µm) and (b) axis ($Y_i - Y_i'$) (µm), where dashed

lines and solid lines are the results from the test rig and machine tool, respectively.

C. Dual-sensor autofocusing comparison on two machines

The procedure of autofocusing, image-capturing, image processing and centroid position detection was carried out five times to evaluate the average of the deviations and the repeatability in micrometres, based on the conversion factor *k*. On the test rig, *k* was calibrated as 2.3012 μm/pixel for the CCD camera of 768×576 pixels at 3.5 times amplification of the optical microscope. On the machine tool, *k* was calibrated as 0.6410 μm/pixel for the CCD camera of 2560×1920 pixels at 3.75 times amplification of the optical microscope. The measurement results are shown in Fig.12 (a) and (b), where the centroid deviations ($X_i - X_i'$) and ($Y_i - Y_i'$) represent the deviation from the datum hole, located at 0°. The detailed average $\overline{\Delta X}$ and $\overline{\Delta Y}$ of centroid deviations and repeatability (σ) of five repeated measurements are listed in table 2 and 3. The largest non-repeatability takes place at the 270° hole, due to the broken drill inside. Additional image-processing capability could be incorporated into the system to detect such artefacts automatically.

Table 2 average $\overline{\Delta X}$ and repeatability (σ) of centroid deviations in circumferential direction, ($X_i - X_i'$).

Hole legends (at angle)	Images on test rig		Images on machine tool	
	$\overline{\Delta X}$ (μm)	σ (μm)	$\overline{\Delta X}$ (μm)	σ (μm)
0	0	0	0	0
30	-32.2	4.8	-41.2	0.7
60	-23.5	18.7	-374.0	0.5
90	-34.7	20.1	-449.5	6.9
120	37.0	13.7	-394.9	22.0
150	200.4	7.0	-308.2	10.5
180	276.3	5.6	-249.1	3.0
210	166.7	11.1	-310.9	1.2
240	-51.7	9.0	-463.8	2.9
270	-147.7	21.2	-487.3	1.9
300	-160.6	16.4	-391.9	10.6
330	-24.0	6.7	-215.5	4.3
360	1.8	4.0	0.4	0.9

Table 3 average $\overline{\Delta Y}$ and repeatability (σ) of centroid deviations in axis direction ($Y_i - Y_i'$).

Hole legends (at angle)	Images on test rig		Images on machine tool	
	$\overline{\Delta Y}$ (μm)	σ (μm)	$\overline{\Delta Y}$ (μm)	σ (μm)
0	0	0	0	0
30	16.9	13.9	43.0	0.5
60	44.1	6.6	71.8	0.2
90	43.9	5.7	82.0	2.1
120	45.6	2.8	104.8	1.5
150	32.1	1.8	121.4	1.5
180	-1.4	6.6	104.5	1.1
210	-9.0	12.8	89.2	0.4
240	-19.3	11.3	54.6	0.3
270	-41.6	20.9	9.5	0.8
300	-6.5	2.5	29.8	0.5
330	5.5	3.2	24.9	0.7
360	0.5	1.1	0.0	0.8

The maximum non-concentricity between the centreline of the workpiece and that of the rotary stage in the test rig differs from that between the centreline of workpiece and that of rotary indexer in the machine tool in value and at angular position. Consequently, the averages of centroid deviations in the circumferential direction of the two groups of hole images are different. The position errors of the holes merge into the centroid deviations, which remain to be extracted, based on further mathematical analysis and experimental testing. Before that, the averages of the centroid deviations are not comparable. However, the repeatability of the centroid deviations is comparable. The two repeatability values are close to each other in the circumferential direction, as shown in table 2. They differ from each other in the axis direction of the workpiece, highlighting the axial run-out. The elliptical cylinder is connected to the rotary table on the test rig through a thread connection, whilst it is clamped into the rotary indexer on the machine tool by a three-jaw chuck.

7. Conclusion

The ability to measure the position errors of small features rapidly and automatically is highly desirable in precision manufacturing, especially in the aerospace sector, where large patterns of small air-cooling holes are typically found on the freeform surface of aero-engine blades.

Optical evaluation functions, such as the discrete cosine transformation (DCT), are often used to automatically focus by the optical sensor used for measurement. However, this paper has demonstrated that the method does not transfer well to parts with complex geometries. The dual-sensor autofocusing method is proposed as a robust alternative to the purely optical method of focussing. Mathematical analyses of the errors and practical validation have shown that the method is very promising for on-machine autofocusing. An added advantage arises if feedback from the evaluation can be applied to the machine controller to compensate the errors in the case where the optical microscope has a very short depth of field (DOF).

The dual-sensor autofocusing method has no perceived disadvantages in terms of measurement time over current autofocusing methods. The DCT method requires many images to be captured at different lens positions around the focal plane, requiring a motor controlled motion stage to carry the optical microscope to implement the process. Although the proposed autofocusing method also needs motor controlled translation stages to carry the dual-sensor unit to move in two planes, experiments have shown that the dual-sensor autofocusing only requires a single tactile-probe touch to establish focal length and a single optical capture to perform the measurement. To perform the dual-sensor autofocusing and measurement on a high precision CNC machine tool will greatly reduce this cycle time.

This paper is concerned only with the autofocussing technique. Evaluation of the images to establish the position errors of the holes, with estimated measurement uncertainty, is the subject of continued research.

Acknowledgements

We thank the UK's Engineering and Physical Sciences Research Council (EPSRC) funding of the EPSRC Centre for Innovative Manufacturing in Advanced Metrology (Grant Ref: EP/I033424/1). Many thanks also to Mr Wenjun Zhang of Changcheng Institute of Metrology & Measurement (CIMM) Beijing and Mr Andrew Bell of the University of Huddersfield for their assistance with this project.

References

1. A. Weckenmann, G. Peggs, and J. Hoffmann, Probing systems for dimensional micro- and nano-metrology, Meas. Sci. Techno. 17, 504-509(2006).
2. http://www.werth.de/en/user-angebot/products/ sensors.html.
3. H. Cao, Chen, K.T.V. Grattan, and Y. Sun, Automatic micro dimension measurement using image processing methods, Measurement 31, 71-76(2002).
4. Z. Fei, J. Guo, and C. Li, A new method for detecting the diameter and spatial location of tiny through-hole, Advanced Materials Research 189-193, 4186-4190(2011).
5. Y. Luo, D. Hu, and T. Gu, Research on real-time error measurement in curve grinding process based on machine vision, IEEE International Technology and Innovation Conference 656-661(2006).
6. H. P. Syahputra, I.J. Ko, Application of image processes to micro-milling process for surface texturing, Int. J. Precis. Eng. Manuf., 14, 1507-1512(2013).
7. A. Zhou, J. Guo, W. Shao, J. Yang, Multipose measurement of surface defects on rotary metal parts with a combined laser-and-camera sensor, Opt. Eng. 52, 104104(2013).
8. R. Yusvana, D. Headon and G. H. Markx, Isolation and measurement of the features of arrays of cel aggregates formed by dielectrophoresis using the user-specified multi regions masking (MRM) technique, J. Physics: Conference Series 183, 012022 (2009).
9. T. Shu, Y. Zheng, Z. Shi, Image processing-based wheel steer angle detection, J. electronic Imaging 22, 043005(2013).
10. F. Shen, L. Hodgson, K. Hahn, Digital autofocus methods for automated microscopy, Methods in Enzymology 414, 620-632(2006).
11. M. Yang, L. Luo. A rapid auto-focus method in automatic microscope, IEEE International Conference on Signal Processing (ICSP), 502-505(2008).
12. C. J. Kuo, C. Chiu, Improved auto-focus search algorithms for CMOS image-sensing module, Journal of Information Science and Engineering 27, 1377-1393 (2011).
13. X. Qiu, and Z.Yang, Study on entropy function optimization problem in auto-focusing algorithm applied for radar imaging, IEEE International Conference on Microwave and Millimeter Wave Technology (ICMMT) 4, 2055-2058(2008)
14. A. B. Mario, Á B Josué, A. Leonardo, and C.María, Fast autofocus algorithm for automated microscopes, Optical Engineering 44, 063601(2005).
15. W. Chen, M. Er, and S. Wu, Illumination compensation and normalization for robust face recognition using discrete cosine transform in logarithm domain, IEEE Transactions on Systems, Man, and Cybernetics, Part B: Cybernetics 36, 458-466(2006).
16. J. He, R. Zhou, and Z. Hong, Modified fast climbing search auto-focus algorithm with adaptive step size searching technique for digital camera, IEEE transactions on Consumer Electronics 49, 257-262(2003).
17. http://www.optiv.net/Multisensor--Optical-Systems_583. htm.
18. X. Chen, A. Longstaff, S. Parkinson, and A. Myers, A method for rapid detection and evaluation of position errors of patterns of small holes on complex curved and freeform surfaces, Int. J. Precis. Eng. Manuf., 15, 209-217(2014).
19. ISO/DIS 230-2, Test code for machine tools – Part 2: Determination of accuracy and repeatability of positioning of numerically controlled axes, ISO (2011).
20. ISO 230-1, Test code for machine tools – Part 1: Geometric accuracy of machines operating under no-load or quasi-static conditions, ISO (2012).
21. A. Jeffrey, Mathematics for engineers and scientists, sixth-edition, Chapman & hall/CRC (2004).